Analytic Free Molecular Aerodynamics for Rapid Propagation of Resident Space Objects

Kenneth A. Hart,* Kyle R. Simonis,† Bradley A. Steinfeldt,‡ and Robert D. Braun§

Georgia Institute of Technology, Atlanta, GA, 30332-1510, USA

Aerodynamic forces and moments are significant perturbations on low-Earth orbiting objects, second in magnitude to the non-spherical gravity field. Traditionally, the aerodynamic perturbations are calculated using a Direct Simulation Monte Carlo (DSMC) Method. Under certain assumptions, these forces and moments can be described analytically via free molecular flow theory. Using symbolic manipulation techniques, exact expressions for the free molecular aerodynamics of analytic shapes can be derived. In this investigation, analytic expressions for the aerodynamic force and moment coefficients of primitive and composite parametric surfaces are derived, then validated against industry-standard DSMC techniques. A framework for the rapid and accurate calculation of free molecular aerodynamics of composite geometries based on superposition is described. This framework is applied to axisymmetric composite geometries. Results within 6% of DSMC calculations are obtained in 0.05% of the time. The analytic aerodynamics models enable rapid trajectory and uncertainty propagation for low-Earth orbiting objects. A case study on aerodynamic perturbations of a LEO nanosatellite is included to demonstrate application of these analytic models. The case study shows that these derived analytical free molecular aerodynamics produce results that are applicable to inclusion in rapid trajectory propagation tools for orbit prediction and conceptual mission design.

Nomenclature

A	Area
C	Coefficient, see subscripts
D	Domain of integration
h	Specific angular momentum
J	Jacobian determinant
Kn	Knudsen Number
l	Length
M	Molar mass
m	Mass
$\boldsymbol{n}$	Normal vector
R	Specific gas constant
$\boldsymbol{r}$	Parameterization
r	Radius
s	Molecular speed ratio
T	Temperature
$\boldsymbol{t}$	Tangent vector
u	First parameterization variable
V	Velocity
v	Second parameterization variable

*Graduate Research Assistant, Daniel Guggenheim School of Aerospace Engineering, AIAA Student Member.
†Undergraduate Research Assistant, Daniel Guggenheim School of Aerospace Engineering, AIAA Student Member.
‡Research Engineer II, Daniel Guggenheim School of Aerospace Engineering, AIAA Member.
§David & Andrew Lewis Professor of Space Technology, Daniel Guggenheim School of Aerospace Engineering, AIAA Fellow.

Subscripts

A	Axial
char	Characteristic
D	Drag
∞	Freestream
L	Lift
l	Roll
m	Pitch
N	Normal
n	Yaw
ref	Reference
S	Side force
T	Tangential
W	Wall
w	Wetted

Symbols

α	Angle of attack
β	Sideslip angle
δ_c	Half cone angle
ε	Specific energy
θ	Angle of incidence
λ	Mean free path
μ	Gravitational parameter
ρ	Density
σ	Accommodation coefficient
τ	Shear

I. Introduction

The collision between two satellites and the Chinese anti-satellite demonstration have motivated improvements to space situation awareness. In-space assets share Earth orbits with decommissioned satellites and other potentially hazardous space debris [1]. Accurate knowledge of and quantified uncertainty in the orbits of all resident space objects (RSOs) must be maintained in order to minimize the probability of future collisions [2]. To predict whether any two of the 20,000 tracked objects will collide, ground-based observations of the objects can be synthesized with accurate models of the dynamics of each object. These dynamics models include the Earth's gravity field, the non-gravitational perturbations of solar radiation pressure, and atmospheric drag.

Many objects in the Space Catalog receive significant perturbing forces due to Earth's atmosphere, which produces aerodynamic forces that act on these bodies [3]. The magnitude of these perturbations can be determined by analytical modeling, repeated observations, or testing. Numerical and experimental data are often more accurate than analytic models; however, run times prohibit characterization of thousands of objects. For missions with a high-fidelity computer-aided design (CAD) model, the numerical approach is preferable over analytic models. For the numerous RSOs with partially-resolved imagery, using DSMC to develop individual aerodynamic databases would require significant computational resources.

A fast and flexible alternative is to analytically model the perturbations, particularly for vehicle geometries that are also analytic. The models are equations that express the forces and moments as functions of the geometry and orientation of the object, as well as atmospheric properties. Recently, analytical expressions for hypersonic continuum aerodynamics have been developed for a variety of shapes, which have enabled rapid propagation of entry trajectories [4, 5, 6]. This general methodology is applied to the free molecular aerodynamics of RSOs and produces results that are comparable to numerical simulation and experimental results and can be included in rapid trajectory propagation tools ideal for conceptual mission design. Analytic aerodynamic models are also useful for identifying aerodynamic parameters, such as the accommodation coefficient, for satellites with simple geometries.

II. Theory

A. Rarefied Gas Dynamics

In general, aerodynamic forces and moments arise from the momentum transferred from a fluid to an object submerged in that fluid. Fluid flows in a manner which conserves three fundamental quantities: mass, momentum, and energy [7, 8]. While the Navier-Stokes equation is valid for continuum flows, the more general Boltzmann equation is appropriate for low-density fluid flow, such as that found in LEO. The primary similarity characteristic of a rarefied flow is its Knudsen number, defined in Eq. (1) as the ratio between the mean free path of the gas, λ, and the characteristic dimension, l_{char}, of the object. The effect of Knudsen number on the characteristics of the flow is shown in Figure 1.

$$\text{Kn} = \frac{\lambda}{l_{\text{char}}} \tag{1}$$

The rarefied regime is loosely partitioned into several sub-regimes based on the rarefaction of the fluid. These sub-regimes include transition, slip, and free molecular flow. Free molecular flow is extremely rarefied, such that the mean free path of the fluid is several times larger than the characteristic length of the object [9]. There is no distinct Knudsen number boundary on free molecular flow. Conservatively, flows where the Knudsen number is greater than 10 are assumed free molecular.

The primary assumption of free molecular flow is that the reflected particles of the fluid have no effect on the freestream [10]. For a flat plate at an angle of attack relative to the freestream, this assumption implies that the flow reflected from the leading edge does not disturb the flow incident on the trailing edge. Another consequence of this assumption is that the boundary layer is very weak and does not affect the reflection of particles from the body.

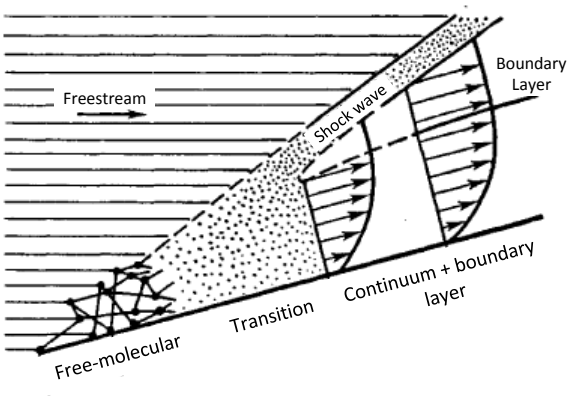

Figure 1. Flow behavior change from hypersonic free-molecular to continuum with increasing characteristic length [11].

B. Maxwellian Specular & Diffuse Model

Maxwell considered total number of gas-surface collisions to be divided into two categories: specular reflections and diffuse reflections [12]. In this model, a fraction of the collisions, σ, are diffuse and the remainder, $1-\sigma$, are specular. The pressure and shear coefficients have been derived in several sources and are reproduced in Eqs. (2) and (3) [9].

$$\begin{aligned} C_p = {} & (2-\sigma_N)\left(\frac{1}{s^2}\left[\frac{s\sin\theta}{\sqrt{\pi}}e^{-(s\sin\theta)^2} + \left(\frac{1}{2}+(s\sin\theta)^2\right)(1+\text{erf}(s\sin\theta))\right]\right) \\ & + \frac{\sigma_N}{2s^2}\sqrt{\frac{T_W}{T_\infty}}\left((s\sin\theta)\sqrt{\pi}[1+\text{erf}(s\sin\theta)] + e^{-(s\sin\theta)^2)}\right) - \frac{1}{s^2} \end{aligned} \tag{2}$$

$$C_\tau = -\frac{\sigma_T\cos\theta}{s}\left(\frac{1}{\sqrt{\pi}}e^{-(s\sin\theta)^2} + (s\sin\theta)[1+\text{erf}(s\sin\theta)]\right) \tag{3}$$

$$s = \frac{V_\infty}{\sqrt{2RT_\infty}} \tag{4}$$

These pressure and shear coefficient expressions are valid for any flow which is sufficiently rarefied. They are based on the following assumptions: (1) the freestream is undisturbed by the reflected particles, (2) the accommodation coefficients represent the average distribution of the specular and diffuse reflections, and (3) the diffuse reflection velocities are Maxwellian distributed. The first assumption is equivalent to assuming a Knudsen number greater than 10.

C. Surface Integration

Integrating these infinitesimal forces across parametric surfaces has been attempted in the past, though closed-form solutions were difficult to derive even for simple geometries [13, 14]. Since the pressure and shear coefficients are themselves volume integrals over the velocity space, a closed-form surface integral of these quantities adds complexity to the problem. In some cases, closed-form expressions were derived by restricting the applicability, such as a cone at a total angle of attack less than the half-cone angle [10].

Recent advances in computer algebra systems have enabled a more thorough search for solutions to these surface integral expressions. As a result, the derived analytic aerodynamics are free of orientation restrictions. Furthermore, there are no additional regime restrictions imposed on these solutions beyond what has been assumed in the derivation of the pressure and shear coefficients given in Eqs. (2) and (3).

The following quantities are defined on a general surface: the surface normal vector, the Jacobian determinant, the surface tangent vector, and the angle of incidence. These quantities are given respectively in Eqs. (5), (6), (7) and (8), where u and v are the parameters of $\boldsymbol{r}$ and are ordered such that $\boldsymbol{n}$ is outward facing.

$$\boldsymbol{n} = \frac{\partial \boldsymbol{r}}{\partial u} \times \frac{\partial \boldsymbol{r}}{\partial v} \tag{5}$$

$$J = ||\boldsymbol{n}||_2 \tag{6}$$

$$\boldsymbol{t} = \hat{\boldsymbol{n}} \times \left(-\hat{\boldsymbol{V}}_\infty \times \hat{\boldsymbol{n}} \right) \tag{7}$$

$$\sin\theta = -\hat{\boldsymbol{V}}_\infty \cdot \hat{\boldsymbol{n}} \tag{8}$$

The normal vector $\boldsymbol{n}$ points along the first basis vector defined in the previous section, while the tangent vector $\boldsymbol{t}$ points along the second basis vector. Combining these vector definitions with the pressure and shear coefficient equations results in the expressions given in Eqs. (9) and (10) for the force and moment coefficients expressed in the body frame.

$$\begin{pmatrix} C_A \\ C_S \\ C_N \end{pmatrix} = \frac{1}{A_{\text{ref}}} \iint_{A_w} C_p \hat{\boldsymbol{n}} + C_\tau \hat{\boldsymbol{t}} \, \mathrm{d}A \tag{9}$$

$$\begin{pmatrix} C_l \\ C_m \\ C_n \end{pmatrix} = \frac{1}{A_{\text{ref}} \; l_{\text{ref}}} \iint_{A_w} \boldsymbol{r} \times \left(C_p \hat{\boldsymbol{n}} + C_\tau \hat{\boldsymbol{t}} \right) \, \mathrm{d}A \tag{10}$$

The domains of integration in these expressions are the locus of points on the surface that are apparent to the freestream. There are no pressure or shear forces on the leeward portion of the surface. The domain of integration is every point on the surface where the sine of the incidence angle, θ, is non-negative.

III. Results and Validation for Primitive Shapes

Analytic free molecular aerodynamic expressions are developed for the panel, rectangular prism, sphere, cylinder, and cone. The properties of these shapes, including the specifications of the shapes used for validation, are detailed in the following sections. The analytic aerodynamics for these shapes are available through the Supplemental Materials link that accompanies the electronic version of this article at `http://arc.aiaa.org`.

A. Primitive Geometries

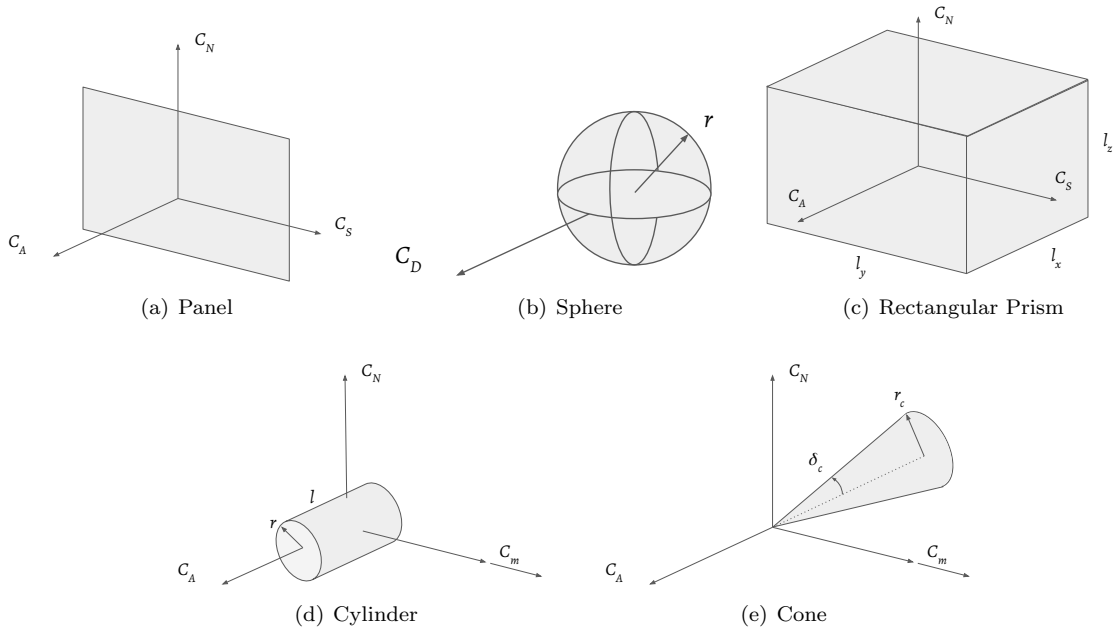

(a) Panel (b) Sphere (c) Rectangular Prism

(d) Cylinder (e) Cone

Figure 2. Diagrams of primitive geometries.

1. Panel

The panel is the interior of a Jordan curve, as shown in Figure 2(a) [15]. The panel can be used to approximate the aerodynamics of RSOs with large solar arrays. Integration is simplified for this geometry by the fact that the infinitesimal force, using Eqs. (2) and (3), is constant across the surface. If the reference area of the panel is equal to the surface area, then the force coefficients are equal to the integrand. The moment integrands evaluate to zero if the center of reference is the centroid of the panel. The panel geometry is included as a reference for the validation results of more complex geometries.

2. Sphere

The free molecular drag on a sphere has been derived previously and it is included in this paper for completeness using the full expressions for C_p and C_τ in Eqs. (2) and (3), respectively [9]. A thorough derivation for the sphere drag coefficient, given in Eq. (11) can be found in the literature [10]. Though this expression is commonly used in LEO drag predictions, the disadvantage of sphere modeling is the absence of lift and side forces, the aerodynamic moments, and stable orientation. In applications such as space situational awareness and RSO trajectory propagation, other geometry models may be more appropriate than the sphere model.

$$C_D = (2 - \sigma_N + \sigma_T)\left(\frac{1}{2} + \frac{1}{2}\mathrm{erf}(s)\left(1 + \frac{1}{s^2} - \frac{1}{4s^4}\right) + \frac{\left(1 + 2s^2\right)e^{-s^2}}{4s^3\sqrt{\pi}}\right) + \frac{\sigma_N}{3s}\sqrt{\frac{\pi T_W}{T_\infty}}(1 + \mathrm{erf}(s)) + \frac{2 - \sigma_N}{2s^2} + \frac{\sigma_N}{6s^4}\left(1 + \left(2s^2 - 1\right)e^{-s^2}\right)\sqrt{\frac{T_W}{T_\infty}} \tag{11}$$

3. Rectangular Prism

The rectangular prism, shown in Figure 2(c), can approximate a wide variety of geometries through its three parameters: l_x, l_y, and l_z. For example, nanosatellites are commonly shaped like rectangular prisms. To generate analytic expressions for the free molecular aerodynamics of a prism, the flat plate equations model the contributions of each face and the Heaviside function switches off the faces that are shadowed. This formulation is similar to a panel code, though it differs in that the analytic expression does not include loops or if statements [7]. The analytic rarefied aerodynamic expressions for the rectangular prism, given in the supplemental materials, include the complete expressions for C_p and C_τ given respectively in Eqs. (2) and (3). For the rectangular prism, the reference area is defined by the y–z cross-sectional area, $l_y\, l_z$, the reference length is defined as l_x, and the moments are taken about the geometric center.

4. Cylinder

The right circular cylinder, shown in Figure 2(d), is defined by two parameters: its radius r and length l. The cylinder geometry can approximate upper stages of rockets, which are a common class of RSOs. In the aerodynamic expressions, the reference area is the cross-sectional area of the cylinder, $\pi\, r^2$, and the reference length is l. The moments are taken about the geometric center of the cylinder. Integration over the cylindrical hull is simplified by symmetry about the x axis and across the y–z plane. The complete expressions for C_p and C_τ given in Eqs. (2) and (3) are used for this geometry. The two circular plates at the ends of the cylinder are incorporated with the Heaviside formulation. The analytic force and moment coefficients in the supplemental materials are valid for any arbitrary angle of attack, whereas previous investigations restricted the angle of attack to specific cases.

5. Cone

The right circular cone, illustrated in Figure 2(e), is constructed from the locus of rays that are a fixed angle from the central axis. Rarefied aerodynamics of the cone and other nosecone geometries have been studied extensively, though past analytic aerodynamic calculations have been restricted to cases where the total angle of attack is less than the cone angle [9]. Analytic expressions for the perturbations on the cone can be manipulated to generate the aerodynamics of a conical frustum as a result of the first fundamental theorem of calculus. Two parameters that fully specify a cone are the cone angle, δ_c, and the base radius r_c. The aerodynamic reference area and length for the cone are $\pi\, r_c^2$ and $r_c \cot \delta_c$, respectively, and the moments are taken about the vertex of the cone. Since the cone is rotationally symmetric about the x-axis, the analytic integration is greatly simplified. The equations in the supplemental materials are valid for any orientation of the freestream, whereas previous formulations required the total angle of attack to be less than the half-cone angle.

B. Validation Method

The expressions for the aerodynamic coefficients are validated primarily against Direct Simulation Monte Carlo (DSMC) numerical simulations. The NASA-developed DSMC Analysis Code (DAC) was used to perform the numerical simulations because it is a high-fidelity rarefied gas flow simulator [16]. Wind tunnel test results for the sphere are compared against the analytic expression for the drag coefficient.

In Eqs. (2) and (3), there are at least eight independent factors that affect the aerodynamic coefficients. A nonlinear sensitivity analysis can provide information regarding which of the factors are most significant. The drag coefficient of a flat plate can be derived from Eq. (9) as a function of the orientation of the freestream, the momentum accommodation coefficients, the freestream velocity, temperature, and molar mass, and the wall temperature. Ranges for these parameters that are relevant to LEO are given in Table 1.

The number density used in all cases is 5×10^{14} m^{-3}, which corresponds to an altitude of approximately 250 km. Collisions were turned on in DAC for all the geometries for consistent results across the simple and composite geometries.

	Input Variable							
Bound	α (deg)	β (deg)	V_∞ (m/s)	T_∞ (K)	M (g/mol)	σ_N	σ_T	T_W (K)
Lower	-90	-90	5500	200	2	0	0	100
Upper	90	90	9500	2000	46	1	1	500

Table 1. Ranges for variables in sensitivity analysis.

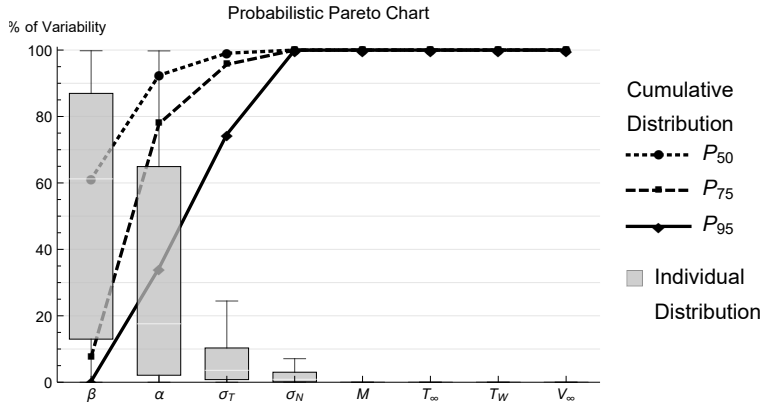

Figure 3. Nonlinear sensitivity analysis of the drag coefficient of a flat plate.

Assuming independent uniform distributions on each of the factors, a Monte Carlo simulation on the gradient of the drag coefficient can show which factors are significant over a LEO-relevant domain. These data are presented in Figure 3 as a probabilistic Pareto chart [17]. The results of this study show that α, β, σ_N, and σ_T are the only significant variables for a flat plate object in LEO. To validate geometries with planes of symmetry, the space of (α, β) can be further reduced.

C. Validation Results

1. Panel

The panel is included in this analysis because it is a fundamental geometry and the primary shape of stereolithography (STL) files, which can be produced by most CAD software. The analytic results are compared to DAC numerical simulation data. In Figure 4, the force coefficients of the panel are illustrated with the angle of attack swept and the sideslip angle fixed at zero. The data points in these plots are the results from DAC and the solid lines are the analytic solution. The maximum percent error between them is 0.5%, as shown in Figure 11.

2. Sphere

The analytic expression for drag on a sphere was validated against both DAC numerical simulations and against experimental results. Figure 5(a) shows the drag on a sphere as computed by DAC and by the analytic model [18]. Figure 5(b) shows a comparison of the analytic model against wind tunnel test results [19]. The percent errors for the sphere are given in Figure 11 and is less than 0.6%.

3. Rectangular Prism

Analytic expressions for a rectangular prism were developed using the Heaviside formulation of the surface integral. The results in Figure 6 are specific to a rectangular prism with parameters $l_x = 3$, $l_y = 1$, and $l_z = 2$ at an angle of attack of 30°. The distribution of percent errors for the prism is given in Figure 11. The

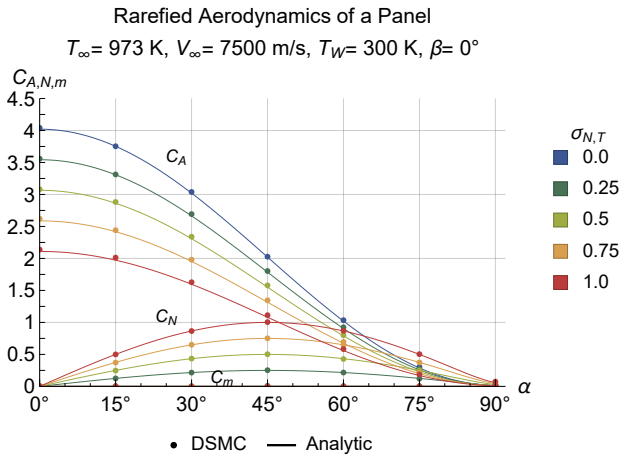

Figure 4. Comparison of the analytic and DAC calculations for the aerodynamic coefficients of a panel.

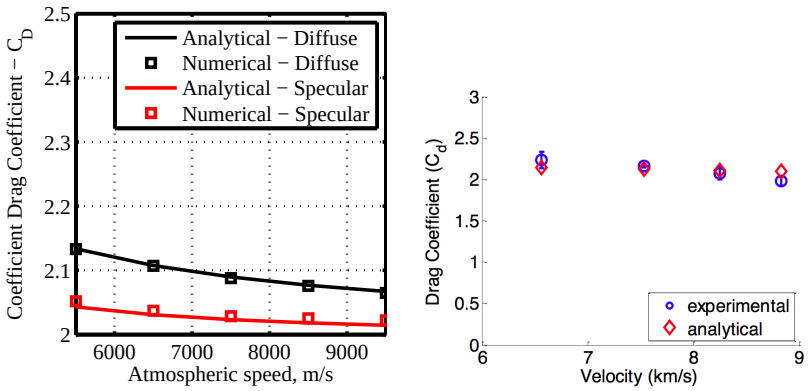

(a) DAC Comparison (b) Experimental Comparison

Figure 5. Validation of the rarefied aerodynamic drag coefficient of a sphere.

maximum percent error is less than 3%. The aerodynamics for prisms with different parameters at different orientations can be calculated from the analytic expressions.

4. Cylinder

The analytic force and moment coefficients on the cylinder were derived by taking advantage of the axial symmetry of the body. The analytic results for a cylinder with a length-to-diameter ratio of 2.18 are compared to DAC numerical simulation data in Figure 7(a). The percent error distribution for the cylinder is shown in Figure 11 and is less than 5%. Because the figure is axisymmetric, α represents the total angle of attack. Several combinations of specular and diffuse reflections are shown together to illustrate the range of validity of the analytic model.

5. Cone

A sample case with a 36° half-cone angle was simulated in DAC to validate the analytic expressions. The results for the cone are presented in Figure 7. Overall there is good agreement between the two solutions and the percent error distribution is given in Figure 11. A maximum percent error of 6% is observed. A notable trend in the cone aerodynamics is the relative insensitivity to the accommodation coefficients at low angles of attack. Once the angle of attack passes the cone angle and shadowing occurs, the solutions for different accommodation coefficient values start to differ.

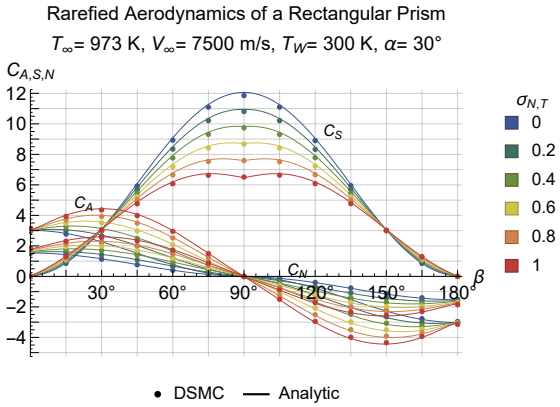

Figure 6. Validation of the aerodynamic coefficients of a rectangular prism.

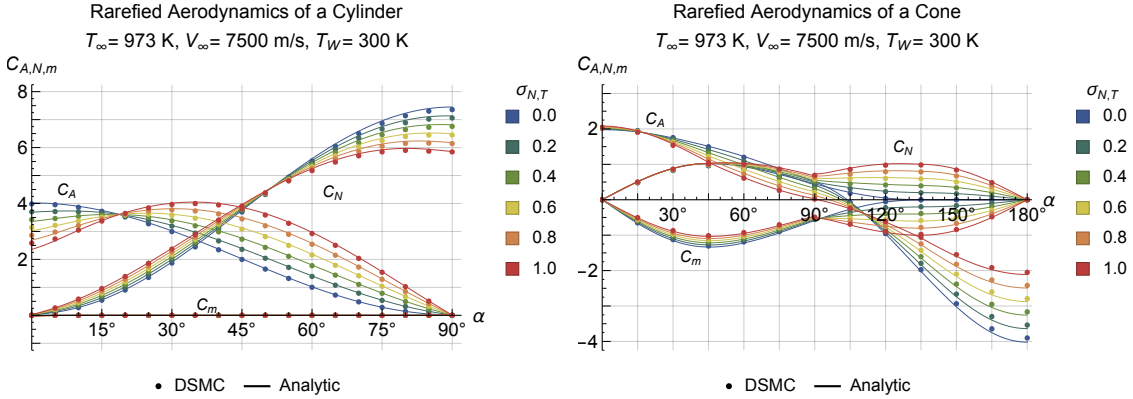

(a) Cylinder, length-to-diameter ratio of 2.18.

(b) Cone, half-cone angle of 36°.

Figure 7. The free molecular aerodynamic coefficients of a cylinder and a cone.

IV. Superposition of Primitive Shapes

A. Mathematical Framework

The geometries in the previous section are good first-order approximations for common RSO geometries, however these shapes could be combined for configurations of greater geometric complexity. In combining the shapes, two phenomena are possible: self-reflection and self-shadowing. Self-reflection occurs when molecules of air can collide with the surface at more than one location. Self-shadowing occurs when a force is not acted on a part of the surface oriented towards the flow because it is in the shadow of another surface. This investigation focuses on the phenomenon of self-shadowing because it can be implemented by restricting the domain of integration. Incorporating self-reflection has been accomplished in some cases, though re-derivation of the infinitesimal force model was required [20, 21]. For generality, only self-shadowing is included in the present superposition framework.

Piecewise surfaces which are locally convex but globally concave exhibit self-shadowing, where part of the surface could be invisible to the flow despite orientation toward it. To map the shadow from one surface onto another, the locus of shadowed points on the first surface are transported along the freestream vector to the second surface. This defines a curve on the second surface which represents the boundary of the shadow, illustrated in Figure 8. The interior of the shadowed region can be determined by testing points that are not on the shadow boundary. The system of three equations in Eq. (12) has four free variables: a coordinate, p, along $\partial\Omega_{w_1}$, the parameters u and v of Ω_2, and an arbitrary variable t that scales the freestream vector. These three equations, one for each entry in the position vector, are shown graphically in Figure 8 and mathematically in Eq. (12). From these three equations, a relationship between u and v on Ω_2 is derived to

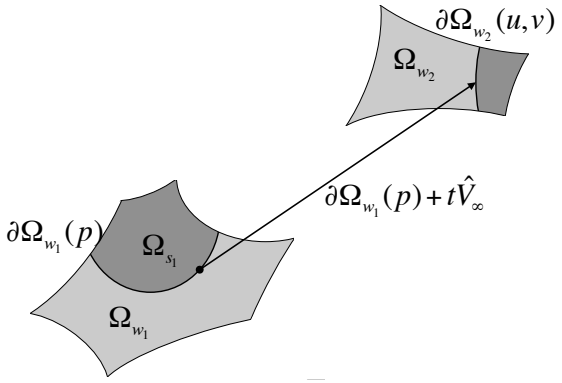

Figure 8. Map of the shadow from one surface onto another.

define the shadow boundary.

$$\partial\Omega_{w_2}(u,v) = \partial\Omega_{w_1}(p) + t\hat{\boldsymbol{V}}_{\boldsymbol{\infty}} \tag{12}$$

The expression in Eq. (12) is an analytic ray-tracing technique that can be applied in reverse to determine the boundary on Ω_1 of the shadow from Ω_2. Any number of surfaces can be included in a model, and in general for n independent surfaces there are $n(n-1)$ shadowing combinations. In the axisymmetric applications below, there are substantially fewer than $n(n-1)$ shadowing combinations. For example, the stepped cylinder has 5 unique parameterized surfaces but only 2 shadowing combinations. This sparseness is due to the fact that shadowing is not mathematically possible in many cases, like the panel on the front of the stepped cylinder cannot shadow the panel on the back. In any case where there are multiple shadows on one surface, the domain of integration becomes all points in D which are neither in the surface's natural shadow nor in the union of the shadows from all other surfaces. The ith domain of integration for a model composed of n surfaces can be expressed by Eq. (13). Since the integral is a linear operator, the sum over all the unique surfaces can be moved outside of the integral as shown in Eq. (14). This technique is applied in the following sections to derive expressions for the free molecular aerodynamics of composite geometries.

$$D_{w_i} = \{(u,v) \in D_i \backslash \bigcup_{j\in\{1,2,\ldots,n\}} D_{s_{j\to i}}\} \tag{13}$$

$$\iint_{D_w} d\boldsymbol{f} = \sum_{i=1}^{n} \iint_{D_{w,i}} d\boldsymbol{f}_i \tag{14}$$

B. Composite Geometries

The analytic aerodynamics for these composite shapes are available through the Supplemental Materials link that accompanies the electronic version of this article at `http://arc.aiaa.org`.

1. Stepped Cylinder

The stepped cylinder, shown in Figure 9(a), is geometrically defined by two non-intersecting coaxial cylinders joined at their planar surfaces. The geometry is axisymmetric, so the derivation of the aerodynamic coefficients assumes that the freestream velocity is in the x–r plane. This configuration has 5 parameterized surfaces: the forward panel, the forward cylindrical hull, the center panel, the aft cylindrical hull, and the aft panel. It is assumed that the aft radius is greater than the forward radius, since the converse can be handled by changing the freestream direction.

A complete derivation of the shadow mappings in the stepped cylinder is in the literature [23]. One of the geometric assumptions that was required to derive closed-form expressions was in the case where the the aft cylinder casts a shadow onto the forward cylinder. The forward cylinder's parameterization is given by distance along the cylinder, u, and an angle, v. The shadow mapping results in the expression given in Eq. (15), which results in a v-integral with no closed form. To achieve closed form, it is assumed that u

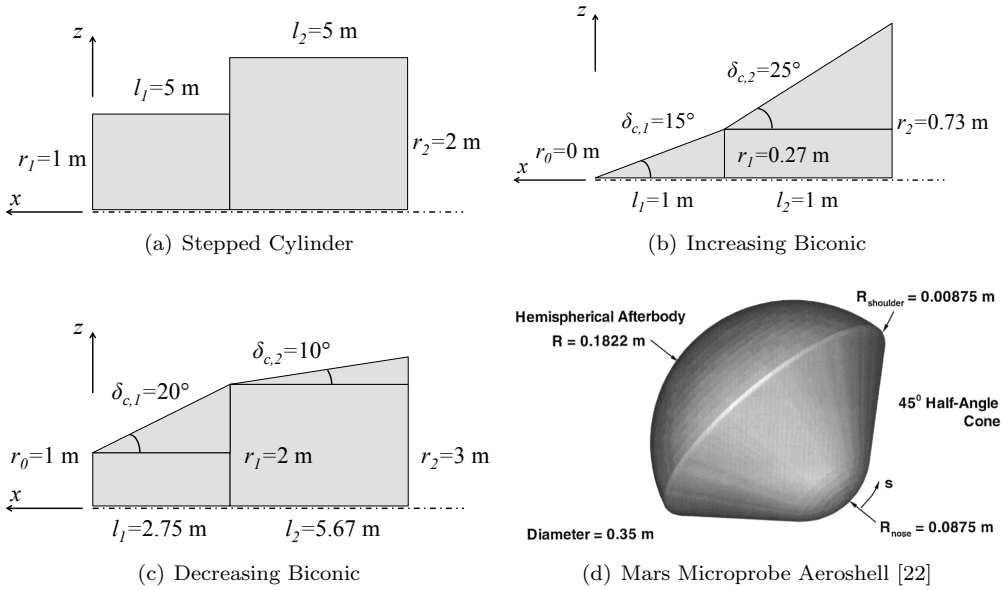

(a) Stepped Cylinder (b) Increasing Biconic

(c) Decreasing Biconic (d) Mars Microprobe Aeroshell [22]

Figure 9. Validation geometries for analytic aerodynamic coefficients.

is constant in v, shown in Eq. (16). For large values of v, this approximation overestimates the size of the shadowed region, though the angle of incidence in this region is small and the contribution to the overall coefficients is insignificant. This is demonstrated in Figure 10(a) in the range from 90° to 180° angle of attack, where there are no significant deviations between the analytic and DSMC solutions.

$$u = l_1 + \cot\alpha \left(\sqrt{r_2^2 - r_1^2 \sin^2 v} + r_1 \cos v \right) \tag{15}$$

$$u \approx l_1 + \cot\alpha \sqrt{r_2^2 - r_1^2} \tag{16}$$

2. Biconic

The biconic geometry, shown in Figures 9(b) and 9(c), is a conical frustum followed by a second frustum of a different cone angle. Whether the cone angle of the aft frustum is greater than or less than that of the forward frustum will result in different shadow mappings. In the case where the cone angle increases, the forward frustum casts a shadow onto the aft frustum and reflects air molecules onto it. For a decreasing cone angle, the two frustums can be superimposed without loss of fidelity because self-reflection cannot occur and the shadow from the first frustum is entirely contained within the shadow of the aft frustum.

A complete derivation of the mappings is available in the literature with two simplifications in the case of the increasing biconic [23]. The first is geometric, where the circumferential limits of integration are the same as those on the first conic. These limits are given by Eq. (17). The second simplification is that the hyperthermal limit is applied to enable a closed-form expression [7]. This limit restricts the applicability of the expressions to flows where the molecular speed ratio, defined in Eq. (4), is greater than 10.

$$v = \pm \mathrm{Re}\left(\cos^{-1}\left(-\cot(\alpha)\tan\left(\delta_{c_1}\right)\right)\right) \tag{17}$$

3. Arbitrary Axisymmetric Geometry

The methodology for combining two shape primitives can be extended to any number of primitives to approximate an arbitrary axisymmetric geometry. For such shapes, the distance from the centerline is a function, F, of axial position. Approximating this function with piecewise-constant values yields a stepped cylinder geometry. Using a piecewise-linear approximation to the radius function would yield a surface composed of conical frustums. Consider a surface of revolution defined by Eq. (18). The function F can be

sampled at a list of u values, and between the samplings the function is approximately linear as shown in Eq. (19). Since the integral is a linear operator, the equations for the force and moment coefficients can be evaluated on the ith interval and summed to obtain an expression for entire surface.

$$\boldsymbol{r} = [u, \quad F(u)\sin v_1, \quad F(u)\cos v_1]^\intercal \tag{18}$$

$$F(u) \approx \begin{cases} F_1 + \frac{u-u_1}{u_2-u_1}(F_2 - F_1) & u_1 \leq u < u_2 \\ F_2 + \frac{u-u_2}{u_3-u_2}(F_3 - F_2) & u_2 \leq u < u_3 \\ \dots & \dots \\ F_i + \frac{u-u_i}{u_{i+1}-u_i}(F_{i+1} - F_i) & u_i \leq u < u_i + 1 \\ \dots & \dots \\ F_{n-1} + \frac{u-u_{n-1}}{u_n-u_{n-1}}(F_n - F_{n-1}) & u_{n-1} \leq u < u_n \end{cases} \tag{19}$$

The assumptions made in generating the biconic and stepped cylinder equations tend to break down when there is a significant variation in the properties of each element. This approximation is appropriate for radius functions that are piecewise smooth and have a continuous derivative. Generally, if the radius function has a monotonically decreasing derivative, then approximating the surface with a series of conical frustums will produce aerodynamic coefficients without a loss of model fidelity.

C. Superposition Validation

1. Stepped Cylinder

An aerodynamic database for the stepped cylinder shown in Figure 10(a) was generated using the analytic models and compared against DAC simulations. The plots show consistent agreement between the analytic model and DAC results. The analytic model does not include self-reflection of molecules, a feature that is apparent in the purely specular axial force coefficient data. In this case, some of the molecules that collide with the side of the first cylinder are also colliding with the front of the second cylinder, which increases the axial force above what the analytic expressions predict. The difference between the analytic and numerical results is less significant for diffuse reflections, which are more common for engineering materials. The two models consistently predict the same values for the aerodynamic coefficients within a 5% difference for more than 80% of the validation points, shown in Figure 11.

2. Increasing Biconic

For the increasing biconic geometry shown in Figure 9(b), there is consistent matching of the DAC and analytic predictions in Figure 10(b). Overall, the magnitude of the error decreases as the accommodation coefficient increases. For diffuse reflections, the analytic and DAC results are within 5% difference as shown in Figure 11. The analytic model also accurately predicts the angles of attack where the coefficients become invariant to the accommodation coefficient, best illustrated in the axial force coefficient plot.

3. Decreasing Biconic

Strong agreement between the analytic and DAC results is shown in Figure 10(c) for the decreasing biconic geometry. The geometry detailed in Figure 9(c) was analyzed as a representative example. At all angle of attacks and accommodation coefficients, the analytic equations predict aerodynamic coefficients that are consistent with the DAC simulations up to 5% according to Figure 11. Of the three elemental superpositions of geometric primitives, the decreasing biconic is the best candidate for the basis of modeling an arbitrary surface of revolution.

4. Arbitrary Conic

The formulation for the arbitrary surface of revolution is applied to the Mars Microprobe aeroshell, shown in Figure 9(d), and compared against published free molecular results in Figure 10(d) [22]. The axial force coefficient at zero angle of attack agrees with the published DSMC results as well. A prominent feature of this figure is the deviation between the two C_N curves near 90° angle of attack. This difference of approximately

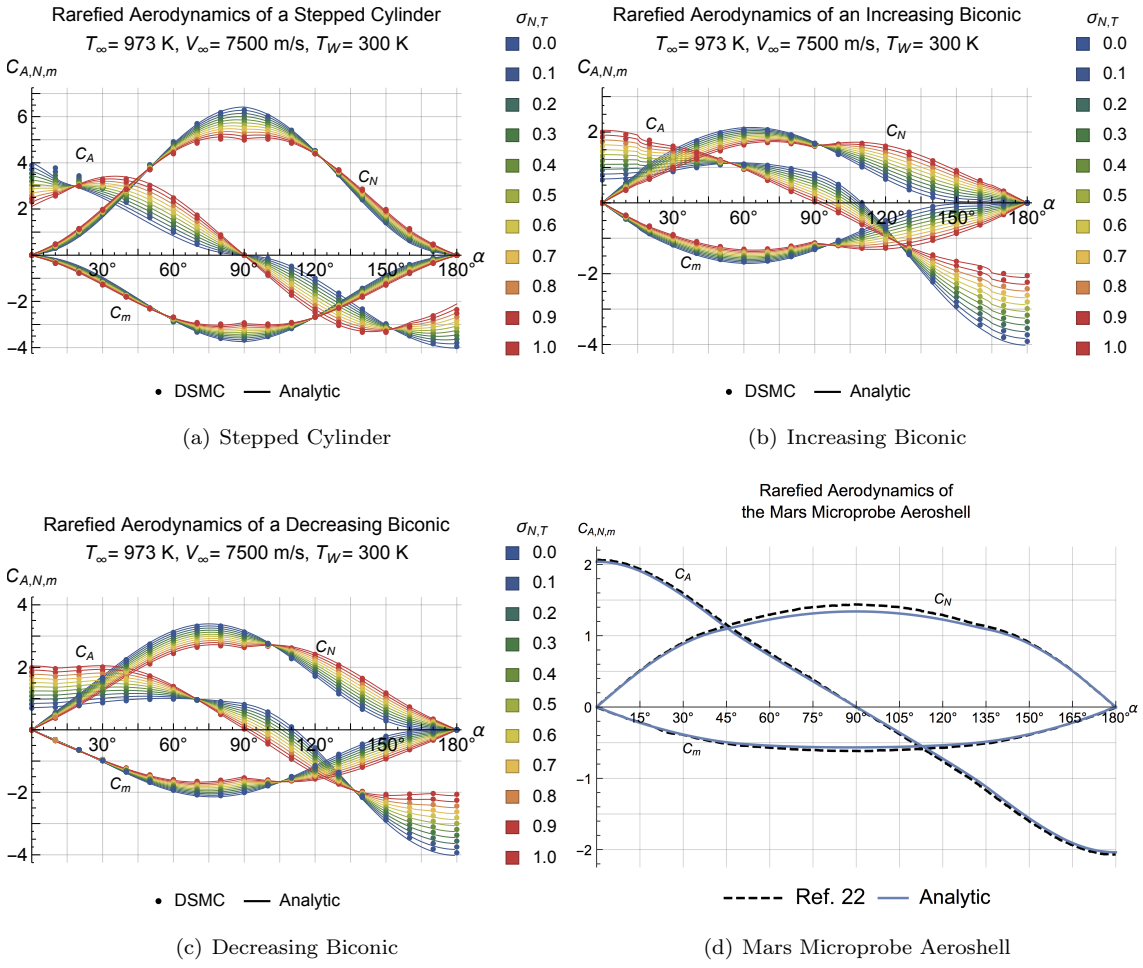

(a) Stepped Cylinder

(b) Increasing Biconic

(c) Decreasing Biconic

(d) Mars Microprobe Aeroshell

Figure 10. Analytic vs numerical comparisons of the free molecular aerodynamics of composite geometries.

8% is caused by differences in the implementation of free-molecular aerodynamics and fidelity of the aeroshell geometry model.

V. Accuracy and Speed

Shown in Figure 11 are the percent errors of the analytic expressions relative to DSMC. The percent errors are aggregated from the data in Figures 4-7 and Figure 10. These errors are within 5% for all of the primitive geometries. For the composite geometries, the biconics are both within 5% but the stepped cylinder and the Mars Microprobe geometries have larger errors in some orientations. The larger errors in the stepped cylinder are primarily due to significant self-reflection at low angles of attack, as shown in Figure 10(a). In the Mars Microprobe aerodynamics, there is an 8% difference in the normal force coefficient at 90° due to differences in the implementation of free-molecular aerodynamics and fidelity of the vehicle geometry model. Overall, the distribution of percent errors in all of these geometries are within 5% when Eqs. (2) and (3) are valid and the geometry does not self-reflect the flow.

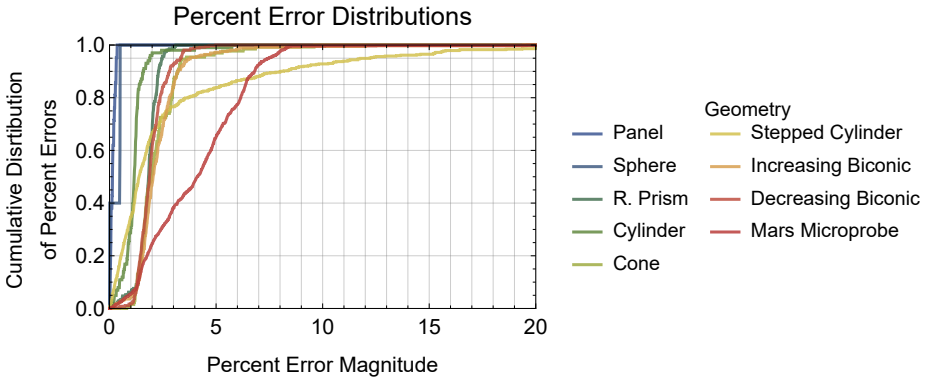

Figure 11. Percent errors for analytical free molecular aerodynamics.

Table 2. Wall times for calculating free molecular aerodynamics.

Geometry	Analytic (s)	DAC (s)
Stepped Cylinder	0.0019	540
Increasing Biconic	0.12	520
Decreasing Biconic	0.092	550
Mars Microprobe	0.30	560

The evaluation times for the analytic expressions and DAC are given in Table 2, for flow oriented along the $-x$ axis and fully diffuse reflections. Reflections were kept on in the DAC runs for consistency, since some of the geometries are concave and could cause particle collisions. The times are valid for a computer with an Intel® Core™ 2 Duo CPU at 2.80 GHz and 4 GB of RAM. These run times are specific to DAC with collisions turned on and do not represent runtimes for other DSMC implementations. In general, a DSMC code requires significantly more floating-point operations than an analytic model. The analytic expressions generally require more time to compute as the complexity of the geometry increases. The times stated for the analytic expressions can vary by 3% and the DAC runs vary by 7%.

VI. LEO Satellite Application

One use case for these analytic expressions is lifetime determination for LEO nanosatellites. An example satellite is shown in Figure 12(a), which has a 3U chassis and two 3Ux3U solar arrays. All new satellite launches are required to have an end-of-life contingency, and for a LEO nanosatellite that is atmospheric reentry. The angle of attack between the satellite and the freestream will determine how much aerodynamic drag will perturb its orbit.

The nanosatellite lift and drag coefficients are derived using the superposition framework. The atmo-

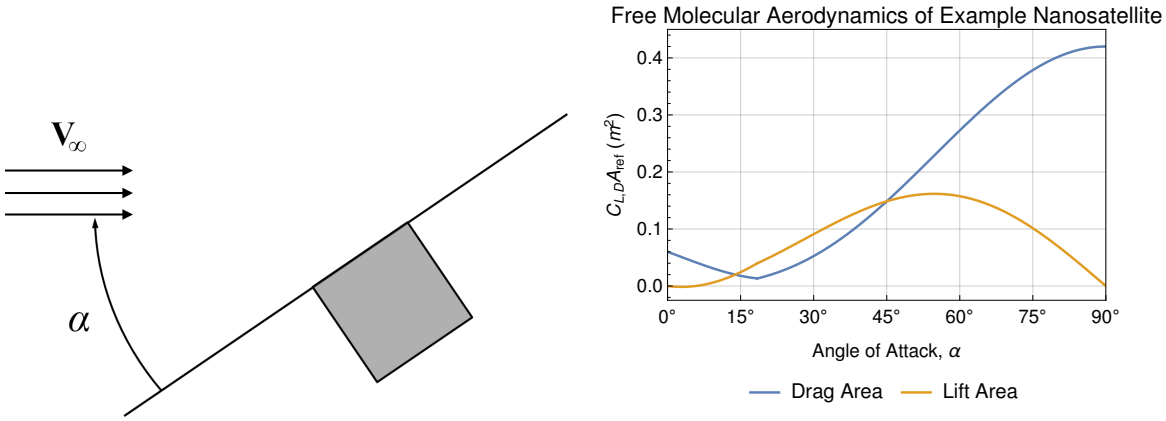

(a) Satellite Configuration

(b) Free Molecular Aerodynamics

Figure 12. Configuration and aerodynamics of a nanosatellite.

spheric conditions in LEO were substituted into these expressions and the surface reflections were assumed to be entirely diffuse, leaving equations for the drag area, $C_D A_{\text{ref}}$, and lift area, $C_L A_{\text{ref}}$, in terms of the angle of attack. These expressions are shown in Figure 12(b). Assuming a fixed attitude, the orbital parameters of this satellite were propagated forward in time, starting at an initial circular altitude of 400 km above the equator and terminating at 100 km. The specific angular momentum and specific energy of the spacecraft are propagated using the equations of motion in Eqs (20) and (21), respectively. The orbit radius, r, and speed, V, are determined through Kepler's first law and the definition of mass-specific energy. The atmospheric temperature, density, and molar mass are modeled with NRLMSISE-00.

$$\dot{h} = -\rho_\infty \left(r\,\varepsilon + \mu\right) \frac{C_D\, A_{\text{ref}}}{m} \tag{20}$$

$$\dot{\varepsilon} = -\rho_\infty \left(\varepsilon + \frac{\mu}{r}\right) V \frac{C_D\, A_{\text{ref}}}{m} \tag{21}$$

In Figure 13(a), the results show that there is a significant advantage to flying with a minimal drag area and that deorbit can be achieved within months by orienting the maximum drag area towards the flow.

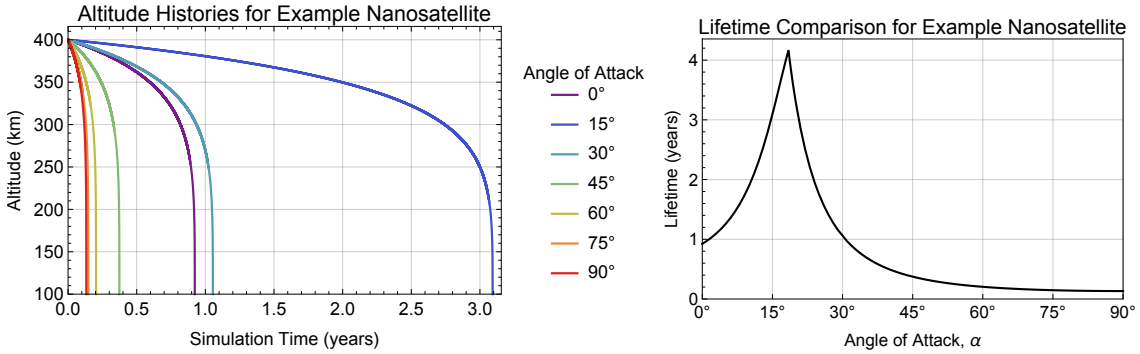

(a) Altitude Histories

(b) Effect of Angle of Attack on Lifetime

Figure 13. Lifetime analysis of the example nanosatellite.

The significant increase in lifetime for $\alpha = 15°$, shown in Figure 13(a), is due to the low drag area of the satellite. At no angle of attack, the satellite chassis is the only drag area on the satellite. As the angle of attack increases, the solar array blocks some of the chassis from the free stream, diminishing the drag area because the angle of incidence on the solar array is small. Eventually the trend reverses and the expected result emerges: increasing the angle of incidence increases the overall drag area. The orientation of the satellite has the effect of reducing the satellite's lifetime from several years to less than one year, a result that could not have been determined using a spherical model for the satellite. The drag minimizing orientation of the

satellite, 18.5° from the freestream, can be found using calculus-based optimization methods on the analytic expression for drag area. To find the drag-minimizing orientation of this geometry using DSMC would be more computationally expensive and not significantly more accurate, considering the difference between the DSMC and analytic models for free molecular flow are within 6% of each other. Generating the results in Figure 13 required approximately 10 seconds using the analytic results, whereas it would have taken approximately 2 hours with DAC.

VII. Conclusions

For primitive geometries and their superposition, integration of analytic expressions for the free molecular pressure and shear coefficients has been shown to produce closed-form expressions for the aerodynamic forces and moments. For primitive geometries, these analytic aerodynamics are valid to within 6% when compared against DSMC and experimental results. Primitive geometries can be combined using superposition to generate the aerodynamics of more complex objects. Using this method, numerical evaluation of the aerodynamics is three orders of magnitude faster than DSMC. Analytical force and moment expressions enable rapid sensitivity analysis. As was shown in the analysis of the lifetime of a LEO nanosatellite, such sensitivity analysis provides a valuable tool for understanding the uncertainty contribution in key variables, such as the accommodation coefficient. In addition, this case study shows the utility of the expressions for rapid trajectory propagation.

Acknowledgments

The work in this paper was funded by Air Force Research Laboratory Contract No. FA9453-13-C-0205.

References

[1] *The Space Report 2014*, The Authoritative Guide to Global Space Activity, The Space Foundation, Colorado Springs, CO, 2014.

[2] Nielsen, P. D., Alfriend, K. T., Bloomfield, M. J., Emmert, J. T., Guo, Y., Maclay, T. D., Miller, J. G., Morris, R. F., Moore, A. B., Russell, R. P., Saari, D. G., Scheeres, D. J., Schonberg, W. P., and Sridharan, R., "Continuing Kepler's Quest," Tech. rep., National Research Council, Washington, DC, 2012.

[3] Kelso, T. S., "Satellite Catalog (SATCAT)," [online database], URL: `https://celestrak.com/satcat`, June 2014.

[4] Grant, M. J. and Braun, R. D., "Analytic Hypersonic Aerodynamics for Conceptial Design of Entry Vehicles," *48th AIAA Aerospace Sciences Meeting Including the New Horizons Forum and Aerospace Exposition*, American Institute of Aeronautics and Astronautics, Orlando, Jan. 2010.

[5] Grant, M. J. and Braun, R. D., "The Extension of Analytic Hypersonic Force Coefficients for Conceptual Design Using the Divergence Theorem," *AIAA Atmospheric Flight Mechanics Conference*, 2012.

[6] Grant, M. J., "The Construction of Analytic Hypersonic Pitch Moment Coefficients Using a Curl Transformation," *51st AIAA Aerospace Sciences Meeting*, American Institute of Aeronautics and Astronautics, Dallas, TX, 2013.

[7] Regan, F. J. and Anandakrishnan, S. M., *Dynamics of Atmospheric Re-Entry*, American Institute of Aeronautics and Astronautics, Reston, VA, 1993.

[8] Bird, G. A., *Molecular Gas Dynamics and the Direct Simulation of Gas Flows*, Oxford University Press, 1994.

[9] Schaaf, S. A. and Chambré, P. L., "Flow of Rarefied Gases," Princeton University Press, Princeton, NJ, 1961.

[10] Sentman, L. H., "Free Molecule Flow Theory and Its Application to the Determination of Aerodynamic Forces," Tech. rep., Lockheed Missiles & Space Company, Sunnyvale, CA, Oct. 1961.

[11] Vallander, S. V., "Collection 1," *Aerodinamika Razrezhennykh Gazov*, 1963.

[12] Maxwell, J. C. and Niven, W. D., "The scientific papers of James Clerk Maxwell. Vol. 2," 1890.

[13] Garfunkel, I. M., "Generalization of Applications of Free Molecule Flow," Tech. Rep. UMR4213, University of Michigan, Ann Arbor, MI, 1950.

[14] Boettcher, R. D. and Legge, H., "Determination of Aerodynamic Forces on Satellites by Theory and Wind-Tunnel Experiments," *Acta Astronautica*, Vol. 7, No. 3, 1980, pp. 255–267.

[15] Do Carmo, M. P., *Differential Geometry of Curves and Surfaces*, Prentice-Hall, Englewood Cliffs, NJ, 1976.

[16] LeBeau, G. J. and Lumpkin III, F. E., "Application highlights of the DSMC Analysis Code (DAC) software for simulating rarefied flows," *Computer Methods in Applied Mechanics and Engineering*, Vol. 191, 2001, pp. 595–609.

[17] Hart Jr, K. A., Steinfeldt, B. A., and Braun, R. D., "Formulation and Applications of a Probabilistic Pareto Chart," *56th AIAA/ASCE/AHS/ASC Structures, Structural Dynamics, and Materials Conference*, American Institute of Aeronautics and Astronautics, Kissimmee, FL, Jan. 2015.

[18] Hart Jr, K. A., Dutta, S., Simonis, K. R., and Steinfeldt, B. A., "Analytically-derived Aerodynamic Force and Moment Coefficients of Resident Space Objects in Free-Molecular Flow," *AIAA Atmospheric Flight Mechanics Conference, National Harbor, MD*, Jan. 2014.

[19] Maldonado, C. A. and Ketsdever, A. D., "Drag Measurements in a Simulated Low-Earth Orbit Environment," *53rd AIAA Aerospace Sciences Meeting*, American Institute of Aeronautics and Astronautics, Kissimmee, FL, Jan. 2015.

[20] Pratt, M. J., "Concave surfaces in free molecule flow," *AIAA Journal*, Vol. 1, No. 7, 1963, pp. 1716–1717.

[21] Schamberg, R., "On Concave Bodies in Free Molecule Flow," The RAND Corporation, 1967.

[22] Mitcheltree, R. A., Moss, J. N., Cheatwood, F. M., Greene, F. A., and Braun, R. D., "Aerodynamics of the Mars Microprobe Entry Vehicles," *Journal of Spacecraft and Rockets*, Vol. 36, No. 3, May 1999, pp. 392–398.

[23] Hart Jr, K. A., Simonis, K. R., Steinfeldt, B. A., and Braun, R. D., "Analytical Aerodynamic Force and Moment Coefficients of Axisymmetric Objects in Rarefied Flow," *AIAA Atmospheric Flight Mechanics Conference*, American Institute of Aeronautics and Astronautics, Kissimmee, FL, Jan. 2015.